Nanoscale

ROYAL SOCIETY OF CHEMISTRY

COMMUNICATION

View Article Online
View Journal | View Issue

Cite this: *Nanoscale*, 2023, **15**, 19469

Received 13th October 2023,
Accepted 9th November 2023

DOI: 10.1039/d3nr05176e

rsc.li/nanoscale

Sub-Ångstrom-scale structural variations in high-entropy oxides†

Hanbin Gao,‡[a,b] Ning Guo,‡[b,c] Yue Gong,[b,c] Lu Bai,[b] Dongwei Wang[b] and Qiang Zheng *[b,c]

High-entropy oxides (HEOs) are a special class of materials that utilize the concept of high-entropy alloys (HEAs) with five or more elements randomly distributing at a single sublattice in near-equiatomic proportions. HEOs have been attracting increasing attention owing to their many outstanding physical and chemical properties. However, unlike HEAs, for which local chemical compositions, order/disorder behaviors, and property–structure relationships have been comprehensively investigated, detailed information on the atomic-scale chemical and structural features and their correlations with functionalities in HEOs so far is still not sufficient. Herein, we select four typical HEOs with pyrochlore, spinel, perovskite and rock-salt type structures, and directly observe and quantify sub-Ångstrom-scale structure variations in different manners by means of advanced aberration-corrected scanning transmission electron microscopy techniques. Visualization and quantification of local structural variations and lattice distortions in the current work may show a valuable example for future investigations on local fluctuating structures and their relationships with properties in more systems of HEOs.

1. Introduction

High-entropy materials are an emergent class of materials that contain five or more elements residing randomly on a single crystallographic site in nearly equiatomic proportions, which were first exploited in alloy systems in 2004, named high-entropy alloys (HEAs).[1] HEAs and the related medium-entropy alloys (MEAs) have been attracting a large amount of interest, due to their unusual and exceptional mechanical performances and potential applications as structural materials.[2–4] Despite containing multiple principal elements, HEAs and MEAs in general crystallize in simple body-centered cubic, face-centered cubic, or hexagonal close-packed structures.[5] HEAs and MEAs were initially considered as random and homogeneous solid solutions with ideal disordering;[6] however, many studies have revealed that variations of local chemical compositions and structures inherently exist in HEAs and MEAs.[7,8] Quantitative characterization studies were thereby carried out to analyze and visualize such short-range ordering behaviors using different techniques, such as pair distribution function (PDF) based on scattering techniques,[8,9] extended X-ray absorption fine structure (EXAFS) technique,[7] transmission electron microscopy (TEM) diffraction and imaging techniques,[10–15] scanning transmission electron microscopy (STEM) imaging and spectroscopy,[3,11,16] atomic probe tomography,[3,12,17] *etc*. Moreover, relationships between degrees of short-range ordering and properties were also investigated comprehensively, suggesting that the mechanical performances of HEAs and MEAs can be tuned and enhanced significantly *via* manipulations of local short-range ordering.[3,10–13,16,17] These insights into special short-range ordering features and relationships between local chemical structures and properties provide great opportunities for tuning atomic-scale compositions and configurations to achieve the desired mechanical properties in HEAs and MEAs.

The concept of HEAs was applied to oxide systems in 2015, and the first high-entropy oxide (HEO) was designed and fabricated based on a rock-salt type structure.[18] Subsequently, high-entropy oxides (HEOs) have been extended to many structural models for traditional oxides, such as perovskites,[19] spinels,[20] and pyrochlores.[21] Meanwhile, similar to HEAs, HEOs also possess many extraordinary physical and chemical properties, including catalysis,[22] colossal dielectric constants,[23] high-capacity retention,[24,25] magnetism,[26,27] and electronic transport.[27] However, compared to HEAs, the structures of HEOs are much more complicated owing to the additional sublattice

[a]*Henan Institute of Advanced Technology, Zhengzhou University, Zhengzhou 450003, China*
[b]*CAS Key Laboratory of Standardization and Measurement for Nanotechnology, CAS Center for Excellence in Nanoscience, National Center for Nanoscience and Technology, Beijing 100190, China. E-mail: zhengq@nanoctr.cn*
[c]*University of Chinese Academy of Sciences, Beijing 101408, China*
†Electronic supplementary information (ESI) available. See DOI: https://doi.org/10.1039/d3nr05176e
‡These authors contributed equally to this work.

of oxygen in their structures, and therefore, despite some studies on the chemical compositions and possible structural variations in HEOs,[18,28–30] investigations on local chemical compositions, atomic configurations, order/disorder behaviors, and possible local lattice distortions in HEOs with these typical crystal structures are still quite lacking, influencing the further establishment of structure–property relationships and potential improvements of HEOs' functionalities.

In this communication, we employ state-of-the-art aberration-corrected scanning transmission electron microscopy imaging and spectroscopy techniques to investigate the atomic-level structure and composition features in four representative HEOs, *e.g.* pyrochlore type $(Yb,Tb,Gd,Dy,Er)_2Ti_2O_7$, spinel type $(Cr,Mn,Fe,Co,Ni)_3O_4$, perovskite type $La(Cr,Mn,Fe,Co,Ni)O_3$, and rock-salt type (Mg,Co,Ni,Cu,Zn)O. Obvious atomic-scale structure variations with different manners, including short-range ordering and B-site displacements, are observed, visualized and quantitatively analyzed among these four types of HEOs. Visualizing and quantifying sub-Ångstrom-scale structural variations in these four types of HEOs may provide insight into future investigations on correlations between local structures and properties and tuning atomic-scale compositions and lattice distortions for exceptional functionalities in the whole family of HEOs.

2. Experimental

A solid-state reaction method was used to prepare single-phase samples for the rock-salt type (Mg,Co,Ni,Cu,Zn)O, pyrochlore type $(Yb,Tb,Gd,Dy,Er)_2Ti_2O_7$, spinel type $(Cr,Mn,Fe,Co,Ni)_3O_4$, and perovskite type $La(Cr,Mn,Fe,Co,Ni)O_3$, following ref. 21 and 31–33. MgO (Alfa Aesar, 99.998%), Co_3O_4 (Alfa Aesar, 99.9985%), NiO (Alfa Aesar, 99.998%), CuO (Alfa Aesar, 99.995%), ZnO (Alfa Aesar, 99.9995%), Yb_2O_3 (Alfa Aesar, 99.9%), Tb_2O_3 (Alfa Aesar, 99.99%), Gd_2O_3 (Alfa Aesar, 99.9%), Dy_2O_3 (Alfa Aesar, 99.99%), Er_2O_3 (Alfa Aesar, 99.99%), TiO_2 (Alfa Aesar, 99.9%), Cr_2O_3 (Alfa Aesar, 99.97%), Fe_2O_3 (Alfa Aesar, 99.9%), MnO (Alfa Aesar, 99.99%), MnO_2 (Alfa Aesar, 99.997%), and La_2O_3 (Alfa Aesar, 99.999%) were used as raw materials. These oxide powders were mixed and ground thoroughly in an equimolar metallic–atomic proportion separately for preparing the four HEO samples. They were pressed into pellets, and heated to 1000 °C, 1400 °C, 1000 °C, and 1400 °C for (Mg,Co,Ni,Cu,Zn)O, $(Yb,Tb,Gd,Dy,Er)_2Ti_2O_7$, $(Cr,Mn,Fe,Co,Ni)_3O_4$, and $La(Cr,Mn,Fe,Co,Ni)O_3$, respectively, in box-type muffle furnaces, and held at these temperatures for more than 10 hours before fast quenching into ice water or liquid nitrogen. The aforementioned processes were repeated several times to obtain sufficiently reacted and uniform HEO samples.

A double-aberration-corrected transmission electron microscope (Spectra 300, Thermo Fisher Scientific Inc.) was utilized to obtain atomic-resolution high-angle annular dark-field (HAADF)-STEM images at an accelerating voltage of 300 kV, with a convergence semi-angle of 25 mrad and a collection semi-angle of 62–200 mrad. Each HAADF image was acquired by stacking 20 fast scanned images (1 μs per pixel dwell time). These images were aligned using phase correlation to reduce the drift between subsequent images before summing. 2D Gaussian fitting was used for acquiring all atomic positions in each HAADF-STEM image. Energy-dispersive X-ray spectroscopy (EDS) data were collected using a Super-X detector.

3. Results and discussion

Four commonly studied HEOs, namely rock-salt type, pyrochlore type, spinel type and perovskite type, were chosen for local structural investigations. Their crystal structures are demonstrated in Fig. 1. Except for the perovskite one that has a distorted cubic structure a with space group of *Pbnm*, the other three types of HEOs all crystallize in cubic structures, with space groups of $Fm\bar{3}m$ (rock-salt type), $Fd\bar{3}m$ (pyrochlore type) and $Fd\bar{3}m$ (spinel type), respectively. In the rock-salt type structure, only one crystallographic site can be occupied by the five cations with an equiatomic ratio. Differently, the other three structures all have two crystallographic sites for cations, which are normally called the A-site and B-site. In this study, we selected rock-salt type (Mg,Co,Ni,Cu,Zn)O and the so-called A-site, mixed A & B-sites and B-site HEOs, respectively, for pyrochlore, spinel, and perovskite type structures, *e.g.* $(Yb,Tb,Gd,Dy,Er)_2Ti_2O_7$, $(Cr,Mn,Fe,Co,Ni)_3O_4$ and $La(Cr,Mn,Fe,Co,Ni)O_3$ for quantitative investigations on atomic-scale structures and compositions. Their XRD patterns and EDS-SEM mapping in Fig. S1–S5 and Tables S1, S2† indicate ideal single phase and micron-scale chemical homogeneity for each sample.

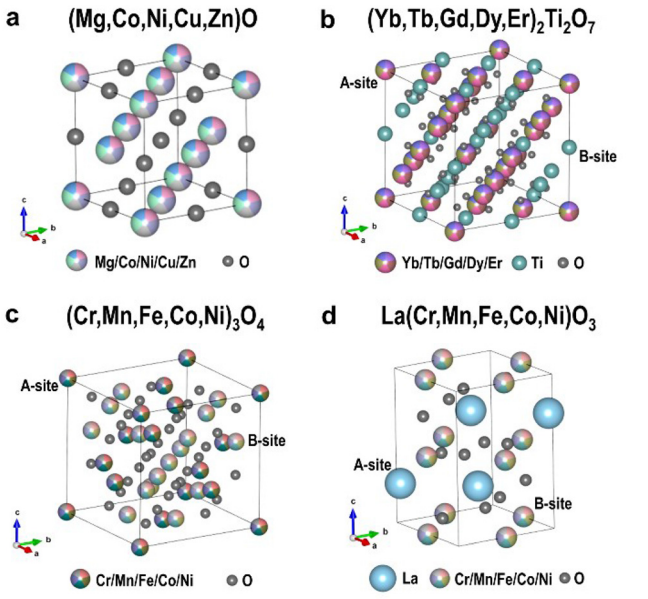

Fig. 1 Crystal structures of (a) rock-salt type (Mg,Co,Ni,Cu,Zn)O, (b) pyrochlore type $(Yb,Tb,Gd,Dy,Er)_2Ti_2O_7$, (c) spinel type $(Cr,Mn,Fe,Co,Ni)_3O_4$, and (d) perovskite type $La(Cr,Mn,Fe,Co,Ni)O_3$.

Local atomic-scale structure features were then investigated based on HAADF-STEM images for the four HEOs. The positions of the atomic columns in HAADF images were obtained using 2D Gaussian fits, and such position acquisition is extremely precise at 1.4 pm, which was estimated from the MgO standard sample (Fig. S6†), following ref. 34 and 35. The aspect ratios or inner angle variations of each quadrangle unit (see Fig. S7†) and local strain maps (Fig. S8 and S9†) were used to evaluate local lattice distortions.

Fig. 2(a) shows a typical HAADF-STEM image in the [100] projection for the rock-salt type (Mg,Co,Ni,Cu,Zn)O HEO. In spite of an apparently perfect cubic structure, each main reflection in its fast Fourier transform (FFT) pattern in the inset is surrounded by two sets of diffuse satellite spots respectively along [011] and [01$\bar{1}$], suggesting the possible appearance of local short-range ordering. Using the refined positions of atomic columns in Fig. 2(a), the uniaxial strain component of x ([010]), y ([001]) and rotation, *i.e.* ε_{xx}, ε_{yy} and ω_{xy}, were analyzed (Fig. S8†), indicating obvious local lattice distortions. To better visualize such distortions, lattice strains in the form of vectors, overlaid on the distribution map of aspect ratios ($l_{[001]}/l_{[010]}$) for all quadrangles in Fig. 2(a), were obtained and are displayed in Fig. 2(b), showing two types of domains in the size range of 1–3 nm. These two types of domains distribute alternately along [011] and [01$\bar{1}$], consistent with the short-range ordering feature in the FFT pattern. Enlargements in Fig. 2(c) reveal that they distort along opposite directions. Moreover, the EDS elemental maps in Fig. 2(d) reveal local chemical fluctuations in this HEO. Such chemical fluctuations, together with local alternating domains, are likely responsible for its short-range ordering behavior. In Fig. 2(e) and (f), similar strain analyses were performed for the MgO standard sample, which reveal a much more uniform and perfect cubic lattice structure. Distributions of the $l_{[001]}/l_{[010]}$ ratios for all quadrangles in Fig. 2(a) and (e) are compared in Fig. 2(g), which shows a much more broadened distribution in (Mg,Co,Ni,Cu,Zn)O, further confirming local lattice distortion in this type of HEO.

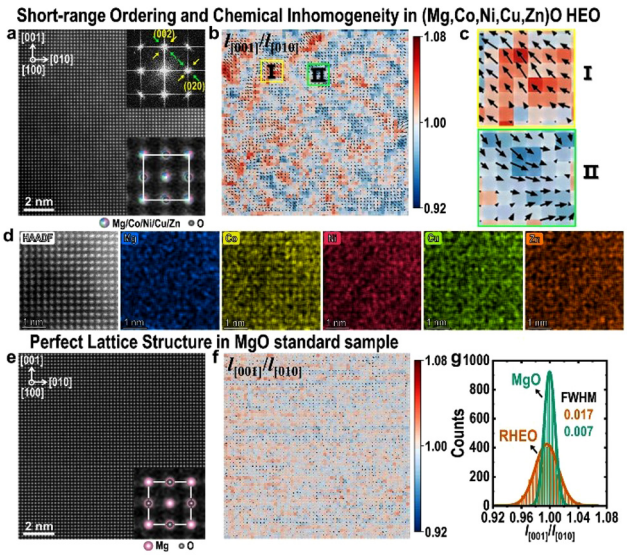

Fig. 2 HAADF-STEM image along the [100] zone axis for the rock-salt type (a) (Mg,Co,Ni,Cu,Zn)O HEO and (e) MgO standard sample with the corresponding FFT pattern in the top inset and the projected structure model at the bottom. (b and f) Lattice strain vectors overlaid on colormaps of the aspect ratios ($l_{[001]}/l_{[010]}$) for all quadrangle units in (a) and (e), respectively. (c) Enlargements of two types of domains in (b). (d) Atomic-resolution EDS elemental maps of Mg, Co, Ni, Cu, and Zn. (g) Comparison between the distributions of aspect ratios for (Mg,Co,Ni,Cu,Zn)O and MgO.

As displayed in Fig. 3(a), a HAADF image for the pyrochlore type $(Yb,Tb,Gd,Dy,Er)_2Ti_2O_7$ HEO along the [100] zone axis is similar to that for the rock-salt type HEO in Fig. 2(a). A-site and B-site cations overlap along this direction. Its FFT pattern in the inset shows weak diffuse spots surrounding the main reflections, respectively, along [010] and [001], again suggesting possible local short-range ordering behavior in this HEO. The strain components of ε_{xx}, ε_{yy} and ω_{xy} were also analyzed (Fig. S9†). Strains in form of vectors, overlaid on the distribution colormap of aspect ratios ($l_{[001]}/l_{[010]}$) for all quadrangles in Fig. 3(a), are exhibited in Fig. 3(b). Obvious local structural distortions from the ideal cubic structure can also be observed, and local alternating domains or clusters in the size of several nanometers emerge in two types of distortion, respectively, along [001] and [010] (Fig. 3(b) and (c)). EDS elemental maps in Fig. 3(d) also reveal local chemical fluctuation in this type of HEO.

Fig. 4(a) exhibits a HAADF image in the projection of [100] for the spinel type $(Cr,Mn,Fe,Co,Ni)_3O_4$ HEO, which involves two types of atomic columns, *i.e.* columns involving A-site cations and columns involving B-site cations and oxygen atoms. In the ideal cubic spinel type structure (a = 8.35 Å), distances of the 1st nearest neighbor (1NN), 2nd nearest neighbor (2NN) and 3rd nearest neighbor (3NN) among these two types of atomic columns should be 1.48 Å, 3.30 Å, and 4.43 Å, respectively. However, in $(Cr,Mn,Fe,Co,Ni)_3O_4$ HEO, obvious

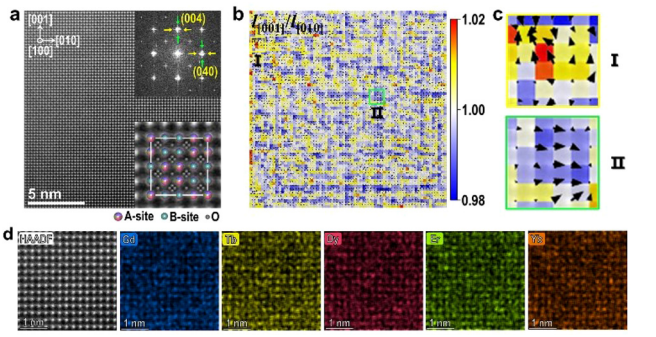

Fig. 3 (a) HAADF-STEM image along the [100] zone axis for the pyrochlore type $(Yb,Tb,Gd,Dy,Er)_2Ti_2O_7$ HEO with the corresponding FFT pattern in the top inset and the projected structure model in the bottom inset. (b) Lattice strain vectors overlaid on colormaps of the aspect ratios ($l_{[001]}/l_{[010]}$) for all quadrangle units in (a). (c) Enlargements of two types of domains in (b). (d) Atomic-resolution EDS elemental maps of Gd, Tb, Dy, Er, and Yb.

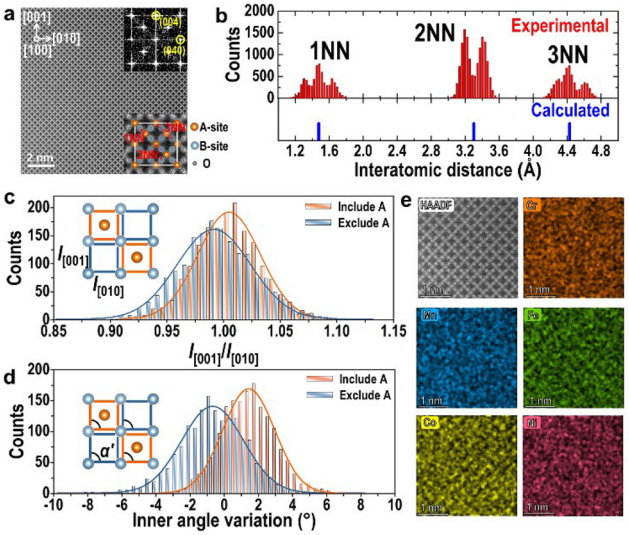

Fig. 4 (a) HAADF-STEM image along the [100] zone axis for the spinel type $(Cr,Mn,Fe,Co,Ni)_3O_4$ HEO with the corresponding FFT pattern in the top inset and the projected structure model in the bottom inset. (b) Splits of 1NN, 2NN and 3NN peaks in distributions of interatomic distances, and calculated distances for them in the ideal cubic spinel structure are compared at the bottom. Statistics of (c) the aspect ratios and (d) the deviation values of inner angles away from 90° for two types of sublattices constructed by atomic columns with B-site cations and oxygen atoms in (a). (e) Atomic-resolution EDS elemental maps of Cr, Mn, Fe, Co, and Ni.

splits of 1NN, 2NN and 3NN peaks in the distributions of interatomic distances in Fig. 4(b) indicate that cations in this structure significantly deviate from their ideal positions. Moreover, since there are two types of quadrangle units, of which one includes columns of A-site cations and the other excludes columns of A-site cations (bottom inset of Fig. 4(a)), distributions of their length ratios and inner angle deviation values are compared in Fig. 4(c) and (d). Interestingly, these two types of sublattices tend to distort in two opposite ways, namely, units involving columns of A-site cations are averagely under compressed strain along [010] and shear strain along [010], while the other type of units undergoes tensile strain along [010] and shear strain along $[0\bar{1}0]$. These two types of units assemble with each other alternating in the real space, resulting in apparently cubic structure on average. EDS elemental maps for the five cations in Fig. 4(e) also reveal local chemical fluctuation in this type of HEO.

Finally, we also investigated the local structure at atomic-scale in the perovskite $La(Cr,Mn,Fe,Co,Ni)O_3$ HEO. This type of HEO crystallizes in an orthodromic structure with a space group of *Pbnm*, and a HAADF image along the [110] direction is displayed in Fig. 5(a). Local structural distortion features can also be observed in this type of HEO, as revealed by the colormaps of aspect ratios ($l_{[001]}/l_{[\bar{1}10]}$) (Fig. 5(b)) and angle deviation (Fig. 5(c)) for all quadrangle units constructed by A-site cations in Fig. 5(a). Besides, similar to the perovskite Ba $(Ti,Sn,Zr,Hf,Nb)O_3$ HEO thin film,[36] B-site displacements exist in this $La(Cr,Mn,Fe,Co,Ni)O_3$ HEO bulk sample, as the vector

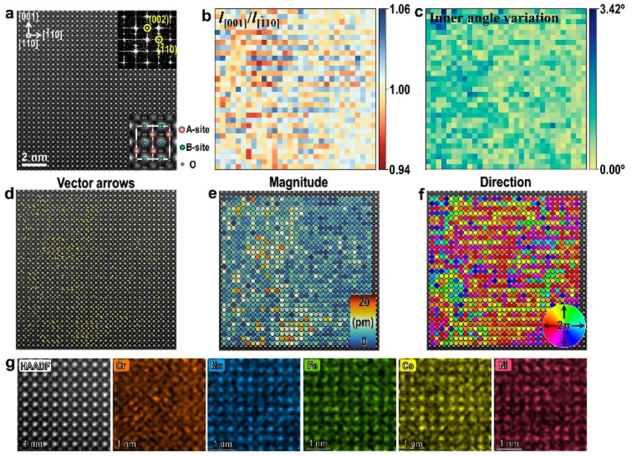

Fig. 5 (a) HAADF-STEM image along the [110] zone axis for the perovskite $La(Cr,Mn,Fe,Co,Ni)O_3$ HEO with the corresponding FFT pattern in the top inset and the projected structure model in the bottom inset. Colormaps of (b) the aspect ratios ($l_{[001]}/l_{[\bar{1}10]}$) and (c) the average absolute deviation values of four inner angles away from 90° for all quadrangle units in (a). B-site displacements: (d) vector arrow map, (e) magnitude map, and (f) direction map. (g) Atomic-resolution EDS elemental maps of Cr, Mn, Fe, Co, and Ni.

arrow map, magnitude map and direction map for displacements of B-site atoms in Fig. 5(a) are demonstrated in Fig. 5(d), (e), and (f), respectively, showing nonuniform displacements with a largest magnitude of 17.3 pm. Local atomic-scale chemical inhomogeneity of B-site cations in Fig. 5(g) may be one possible reason for B-site displacements. Such B-site displacements suggest that the crystal structure of this HEO may deviate from the centrosymmetric structure of *Pbnm* and possible ferroelectricity could also be studied in future work.

4. Conclusions

Atomic-level structures and chemical compositions of rock-salt type (Mg,Co,Ni,Cu,Zn)O, pyrochlore type $(Yb,Tb,Gd,Dy,Er)_2Ti_2O_7$, spinel type $(Cr,Mn,Fe,Co,Ni)_3O_4$, and perovskite type $La(Cr,Mn,Fe,Co,Ni)O_3$ were investigated by means of precise and accurate quantitative STEM techniques. Sub-Ångstrom-scale structural variations and lattice distortions are visualized and quantified in these four types of HEOs, revealing different local distortion manners among them, including short-range ordering and variable B-site displacement, and potential functionalities are also accordingly expected. The observed special local structure variation features may not only expand our understanding on microstructures of HEOs, but also enable us to gain more information on the origins of intriguing functionalities of HEOs.

Author contributions

Hanbin Gao: investigation, characterization, conceptualization, and writing – original draft. Ning Guo: investigation,

characterization, conceptualization, and writing – original draft. Yue Gong: conceptualization, writing – review & editing. Lu Bai: conceptualization, writing – review & editing. Dongwei Wang: writing – review & editing. Qiang Zheng: supervision, investigation, conceptualization, writing – original draft, writing – review & editing, and funding acquisition.

Conflicts of interest

There are no conflicts of interest to declare.

Acknowledgements

This work was supported by the National Key R&D Program of China (2021YFA1202801), the Beijing Municipal Natural Science Foundation (Grant No. 1212016), the Strategic Priority Research Program (B) of the Chinese Academy of Sciences (Grant No. XDB36000000), and the CAS Pioneer Hundred Talents Program.

References

1 J.-W. Yeh, S.-K. Chen, S.-J. Lin, J.-Y. Gan, T.-S. Chin, T.-T. Shun, C.-H. Tsau and S.-Y. Chang, *Adv. Eng. Mater.*, 2004, **6**, 299–303.
2 Z. Li, K. G. Pradeep, Y. Deng, D. Raabe and C. C. Tasan, *Nature*, 2016, **534**, 227–230.
3 Z. Lei, X. Liu, Y. Wu, H. Wang, S. Jiang, S. Wang, X. Hui, Y. Wu, B. Gault, P. Kontis, D. Raabe, L. Gu, Q. Zhang, H. Chen, H. Wang, J. Liu, K. An, Q. Zeng, T.-G. Nieh and Z. Lu, *Nature*, 2018, **563**, 546–550.
4 T. Yang, Y. L. Zhao, Y. Tong, Z. B. Jiao, J. Wei, J. X. Cai, X. D. Han, D. Chen, A. Hu, J. J. Kai, K. Lu, Y. Liu and C. T. Liu, *Science*, 2018, **362**, 933–937.
5 X. Wang, W. Guo and Y. Fu, *J. Mater. Chem. A*, 2021, **9**, 663–701.
6 C. Varvenne, G. P. M. Leyson, M. Ghazisaeidi and W. A. Curtin, *Acta Mater.*, 2017, **124**, 660–683.
7 F. X. Zhang, S. Zhao, K. Jin, H. Xue, G. Velisa, H. Bei, R. Huang, J. Y. P. Ko, D. C. Pagan, J. C. Neuefeind, W. J. Weber and Y. Zhang, *Phys. Rev. Lett.*, 2017, **118**, 205501.
8 Y. Ma, Q. Wang, C. Li, L. J. Santodonato, M. Feygenson, C. Dong and P. K. Liaw, *Scr. Mater.*, 2018, **144**, 64–68.
9 L. J. Santodonato, Y. Zhang, M. Feygenson, C. M. Parish, M. C. Gao, R. J. K. Weber, J. C. Neuefeind, Z. Tang and P. K. Liaw, *Nat. Commun.*, 2015, **6**, 5964.
10 R. Zhang, S. Zhao, J. Ding, Y. Chong, T. Jia, C. Ophus, M. Asta, R. O. Ritchie and A. M. Minor, *Nature*, 2020, **581**, 283–287.
11 X. Chen, Q. Wang, Z. Cheng, M. Zhu, H. Zhou, P. Jiang, L. Zhou, Q. Xue, F. Yuan, J. Zhu, X. Wu and E. Ma, *Nature*, 2021, **592**, 712–716.
12 H.-W. Hsiao, R. Feng, H. Ni, K. An, J. D. Poplawsky, P. K. Liaw and J.-M. Zuo, *Nat. Commun.*, 2022, **13**, 6651.
13 J. B. Seol, W.-S. Ko, S. S. Sohn, M. Y. Na, H. J. Chang, Y.-U. Heo, J. G. Kim, H. Sung, Z. Li, E. Pereloma and H. S. Kim, *Nat. Commun.*, 2022, **13**, 6766.
14 J. Wang, P. Jiang, F. Yuan and X. Wu, *Nat. Commun.*, 2022, **13**, 1021.
15 L. Zhou, Q. Wang, J. Wang, X. Chen, P. Jiang, H. Zhou, F. Yuan, X. Wu, Z. Cheng and E. Ma, *Acta Mater.*, 2022, **224**, 117490.
16 Q. Ding, Y. Zhang, X. Chen, X. Fu, D. Chen, S. Chen, L. Gu, F. Wei, H. Bei, Y. Gao, M. Wen, J. Li, Z. Zhang, T. Zhu, R. O. Ritchie and Q. Yu, *Nature*, 2019, **574**, 223–227.
17 S. S. Sohn, A. K. da Silva, Y. Ikeda, F. Körmann, W. Lu, W. S. Choi, B. Gault, D. Ponge, J. Neugebauer and D. Raabe, *Adv. Mater.*, 2019, **31**, 1807142.
18 C. M. Rost, E. Sachet, T. Borman, A. Moballegh, E. C. Dickey, D. Hou, J. L. Jones, S. Curtarolo and J.-P. Maria, *Nat. Commun.*, 2015, **6**, 8485.
19 S. Jiang, T. Hu, J. Gild, N. Zhou, J. Nie, M. Qin, T. Harrington, K. Vecchio and J. Luo, *Scr. Mater.*, 2018, **142**, 116–120.
20 J. Dąbrowa, M. Stygar, A. Mikuła, A. Knapik, K. Mroczka, W. Tejchman, M. Danielewski and M. Martin, *Mater. Lett.*, 2018, **216**, 32–36.
21 C. Kinsler-Fedon, Q. Zheng, Q. Huang, E. S. Choi, J. Yan, H. Zhou, D. Mandrus and V. Keppens, *Phys. Rev. Mater.*, 2020, **4**, 104411.
22 T. Li, Y. Yao, B. H. Ko, Z. Huang, Q. Dong, J. Gao, W. Chen, J. Li, S. Li, X. Wang, R. Shahbazian-Yassar, F. Jiao and L. Hu, *Adv. Funct. Mater.*, 2021, **31**, 2010561.
23 D. Bérardan, S. Franger, D. Dragoe, A. K. Meena and N. Dragoe, *Phys. Status Solidi RRL*, 2016, **10**, 328–333.
24 A. Sarkar, L. Velasco, D. Wang, Q. Wang, G. Talasila, L. Biasi, C. Kübel, T. Brezesinski, S. S. Bhattacharya, H. Hahn and B. Breitung, *Nat. Commun.*, 2018, **9**, 3400.
25 B. Yang, Y. Zhang, H. Pan, W. Si, Q. Zhang, Z. Shen, Y. Yu, S. Lan, F. Meng, Y. Liu, H. Huang, J. He, L. Gu, S. Zhang, L.-Q. Chen, J. Zhu, C.-W. Nan and Y.-H. Lin, *Nat. Mater.*, 2022, **21**, 1074–1080.
26 A. R. Mazza, E. Skoropata, Y. Sharma, J. Lapano, T. W. Heitmann, B. L. Musico, V. Keppens, Z. Gai, J. W. Freeland, T. R. Charlton, M. Brahlek, A. Moreo, E. Dagotto and T. Z. Ward, *Adv. Sci.*, 2022, **9**, 2200391.
27 P. A. Krawczyk, M. Jurczyszyn, J. Pawlak, W. Salamon, P. Baran, A. Kmita, Ł. Gondek, M. Sikora, C. Kapusta, T. Strączek, J. Wyrwa and A. Żywczak, *ACS Appl. Electron. Mater.*, 2020, **2**, 3211–3220.
28 P. B. Meisenheimer, L. D. Williams, S. H. Sung, J. Gim, P. Shafer, G. N. Kotsonis, J.-P. Maria, M. Trassin, R. Hovden, E. Kioupakis and J. T. Heron, *Phys. Rev. Mater.*, 2019, **3**, 104420.
29 H. Chen, W. Lin, Z. Zhang, K. Jie, D. R. Mullins, X. Sang, S.-Z. Yang, C. J. Jafta, C. A. Bridges, X. Hu, R. R. Unocic, J. Fu, P. Zhang and S. Dai, *ACS Mater. Lett.*, 2019, **1**, 83–88.
30 L. Su, H. Huyan, A. Sarkar, W. Gao, X. Yan, C. Addiego, R. Kruk, H. Hahn and X. Pan, *Nat. Commun.*, 2022, **13**, 2358.

31 J. Zhang, J. Yan, S. Calder, Q. Zheng, M. A. McGuire, D. L. Abernathy, Y. Ren, S. H. Lapidus, K. Page, H. Zheng, J. W. Freeland, J. D. Budai and R. P. Hermann, *Chem. Mater.*, 2019, **31**, 3705–3711.

32 Y. Sharma, Q. Zheng, A. R. Mazza, E. Skoropata, T. Heitmann, Z. Gai, B. Musico, P. F. Miceli, B. C. Sales, V. Keppens, M. Brahlek and T. Z. Ward, *Phys. Rev. Mater.*, 2020, **4**, 014404.

33 D. Wang, S. Jiang, C. Duan, J. Mao, Y. Dong, K. Dong, Z. Wang, S. Luo, Y. Liu and X. Qi, *J. Alloys Compd.*, 2020, **844**, 156158.

34 Q. Zheng, N. J. Schreiber, H. Zheng, J. Yan, M. A. McGuire, J. F. Mitchell, M. Chi and B. C. Sales, *Chem. Mater.*, 2018, **30**, 7962–7969.

35 B. H. Savitzky, I. El Baggari, A. S. Admasu, J. Kim, S.-W. Cheong, R. Hovden and L. F. Kourkoutis, *Nat. Commun.*, 2017, **8**, 1883.

36 Y. Sharma, M.-C. Lee, K. C. Pitike, K. K. Mishra, Q. Zheng, X. Gao, B. L. Musico, A. R. Mazza, R. S. Katiyar, V. Keppens, M. Brahlek, D. A. Yarotski, R. P. Prasankumar, A. Chen, V. R. Cooper and T. Z. Ward, *ACS Appl. Mater. Interfaces*, 2022, **14**(9), 11962–11970.